AGU PUBLICATIONS

Geophysical Research Letters

RESEARCH LETTER
10.1002/2014GL062604

Key Points:
- Far-field tsunami waveforms, with phase correction for time delay, were inverted
- Stable moment rate from seismic inversion and stable spatial slip from tsunami and GPS
- Largest slip located downdip near shore well constrained by tsunami and GPS

Supporting Information:
- Figures S1–S4
- Table S1

Correspondence to:
A. R. Gusman,
adit@eri.u-tokyo.ac.jp

Citation:
Gusman, A. R., S. Murotani, K. Satake, M. Heidarzadeh, E. Gunawan, S. Watada, and B. Schurr (2015), Fault slip distribution of the 2014 Iquique, Chile, earthquake estimated from ocean-wide tsunami waveforms and GPS data, *Geophys. Res. Lett.*, *42*, 1053–1060, doi:10.1002/2014GL062604.

Received 22 NOV 2014
Accepted 21 JAN 2015
Accepted article online 24 JAN 2015
Published online 18 FEB 2015

Fault slip distribution of the 2014 Iquique, Chile, earthquake estimated from ocean-wide tsunami waveforms and GPS data

Aditya Riadi Gusman[1], Satoko Murotani[1], Kenji Satake[1], Mohammad Heidarzadeh[1], Endra Gunawan[2], Shingo Watada[1], and Bernd Schurr[3]

[1]Earthquake Research Institute, The University of Tokyo, Tokyo, Japan, [2]Graduate School of Environmental Studies, Nagoya University, Nagoya, Japan, [3]GFZ Helmholtz Centre Potsdam, German Research Centre for Geosciences, Potsdam, Germany

Abstract We applied a new method to compute tsunami Green's functions for slip inversion of the 1 April 2014 Iquique earthquake using both near-field and far-field tsunami waveforms. Inclusion of the effects of the elastic loading of seafloor, compressibility of seawater, and the geopotential variation in the computed Green's functions reproduced the tsunami traveltime delay relative to long-wave simulation and allowed us to use far-field records in tsunami waveform inversion. Multiple time window inversion was applied to tsunami waveforms iteratively until the result resembles the stable moment rate function from teleseismic inversion. We also used GPS data for a joint inversion of tsunami waveforms and coseismic crustal deformation. The major slip region with a size of 100 km × 40 km is located downdip the epicenter at depth ~28 km, regardless of assumed rupture velocities. The total seismic moment estimated from the slip distribution is 1.24×10^{21} N m (M_w 8.0).

1. Introduction

The 2014 Iquique earthquake sequence began with a large foreshock (M_w 6.7) that occurred on 16 March 2014. The main shock, occurred on 1 April 2014 at 23:46:47 (UTC), had a moment magnitude of M_w 8.2 and a hypocenter located at 19.642°S, 70.817°W with a depth of 23 km, according to the USGS (United States Geological Survey). Two days after, on 3 April, the largest aftershock with M_w 7.7 occurred southeast of the main shock epicenter. The 2014 Iquique main shock generated a tsunami that was recorded by Deep-ocean Assessment and Reporting of Tsunamis (DART) buoys [e.g., *Heidarzadeh et al*., 2014] (Figure 1) and tide gauges (Figure 2). Global Positioning System (GPS) networks recorded the coseismic displacement caused by this earthquake [*Schurr et al*., 2014] (Figure 2).

The slip distribution for the 2014 Iquique earthquake has been estimated by teleseismic inversion [*Lay et al*., 2014; *Yagi et al*., 2014], tsunami inversion of offshore DART waveforms [*Lay et al*., 2014; *An et al*., 2014], and a joint inversion of teleseismic, local strong motion records and GPS data [*Schurr et al*., 2014]. The moment magnitudes estimated by these previous studies are in the range of M_w 8.0–8.2.

For tsunami waveform inversions, the linear shallow water wave, whose velocity solely depends on the bathymetry without dispersion, has been assumed to compute the Green's functions [e.g., *Fujii et al*., 2011; *Fujii and Satake*, 2013]. However, the observed tsunami arrivals in the far field are significantly delayed relative to the simulated tsunami waveforms [*Rabinovich et al*., 2011; *Allgeyer and Cummins*, 2014; *Inazu and Saito*, 2013; *Watada et al*., 2014]. In addition, tsunami forerunners in the far field with a reversed polarity were also reported [*Allgeyer and Cummins*, 2014; *Watada et al*., 2014]. In general, arrival time and initial phase of tsunamis are very important for the tsunami waveform inversion. Because of the arrival time delay and polarity reversal, previous studies on the sources of transoceanic tsunamis such as the 2010 Maule, Chile, tsunami [e.g., *Lorito et al*., 2011; *Fujii and Satake*, 2013], the 2011 Tohoku, Japan, tsunami [e.g., *Fujii et al*., 2011; *Gusman et al*., 2012; *Romano et al*., 2012; *Satake et al*., 2013], and the 2014 Iquique, Chile, tsunami [e.g., *An et al*., 2014] did not use the tsunami waveforms in the far field.

Watada et al. [2014] attributed the observed tsunami traveltime delays and the initial negative depressions to the elastic loading of the seafloor, the compressible seawater, and the geopotential variation due to the moving water mass and proposed a method to correct the waveforms of simulated linear shallow water

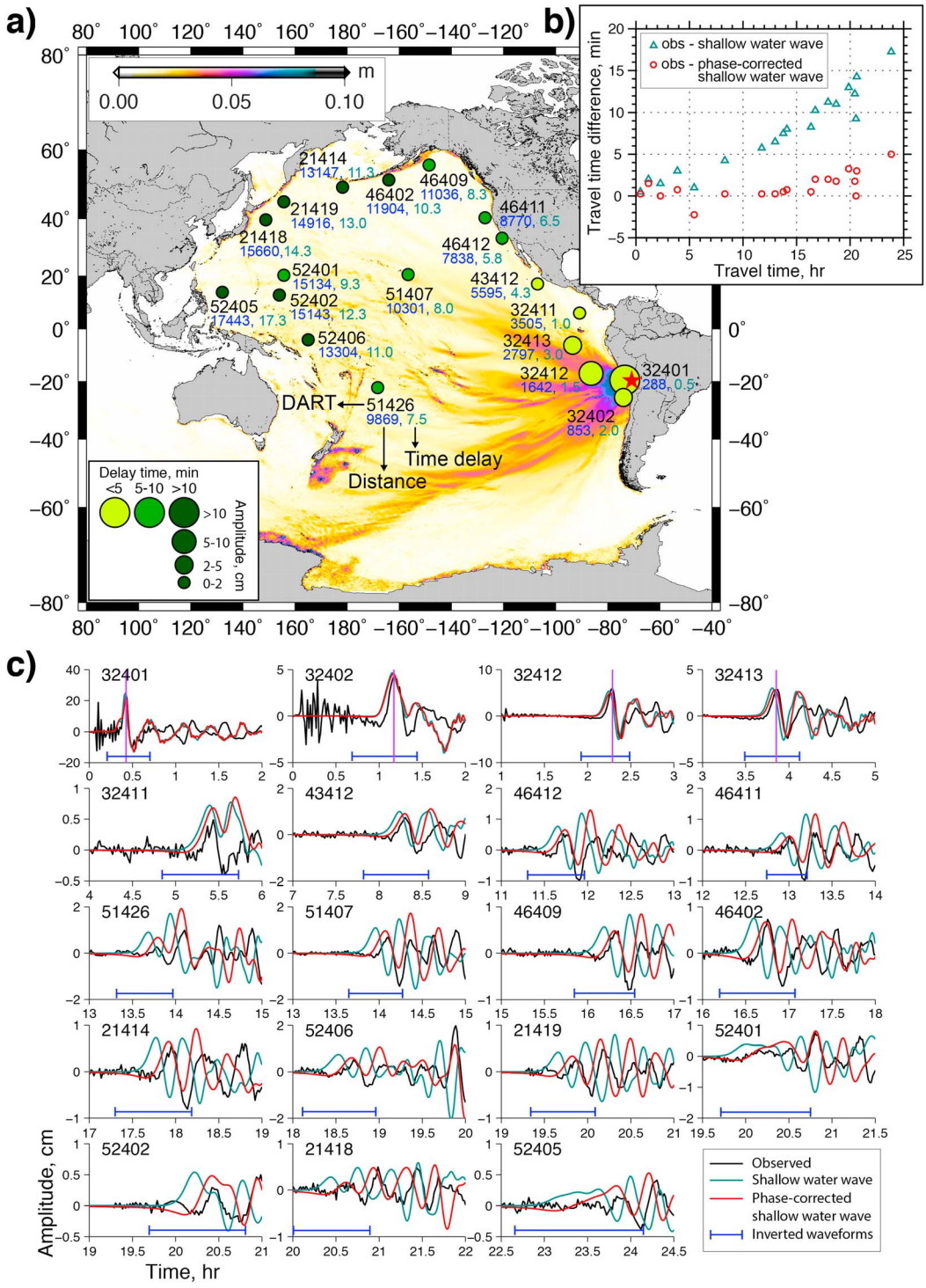

Figure 1. (a) Distribution of maximum simulated tsunami heights from the estimated slip distribution of the 2014 Iquique earthquake from joint inversion of tsunami waveforms and GPS data. Maximum tsunami amplitude at each observation station is indicated by the size of the circle. Green color gradation shows the traveltime delay produced by the shallow water simulation. Station names are indicated by black, blue numbers indicate the distance in kilometers of each station from the epicenter along the great circle, and green numbers indicate the traveltime delay relative to the tsunami shallow water simulation at each station. (b) Traveltime differences between simulated and the observed tsunami waveforms. Green triangles represent traveltime difference between observation and linear shallow water wave. Red circles represent traveltime difference between observation and phase-corrected shallow water wave. (c) Comparison of tsunami waveforms simulated by solving the linear shallow water equations from the estimated slip distribution (green lines), the phase-corrected tsunami waveforms (red lines), and the observed tsunami waveforms (black lines). The blue bars indicate the time range used for tsunami waveform inversion. Purple line marks the observed traveltime of the first tsunami peak, which was used for tsunami back tracing (Figure 2b).

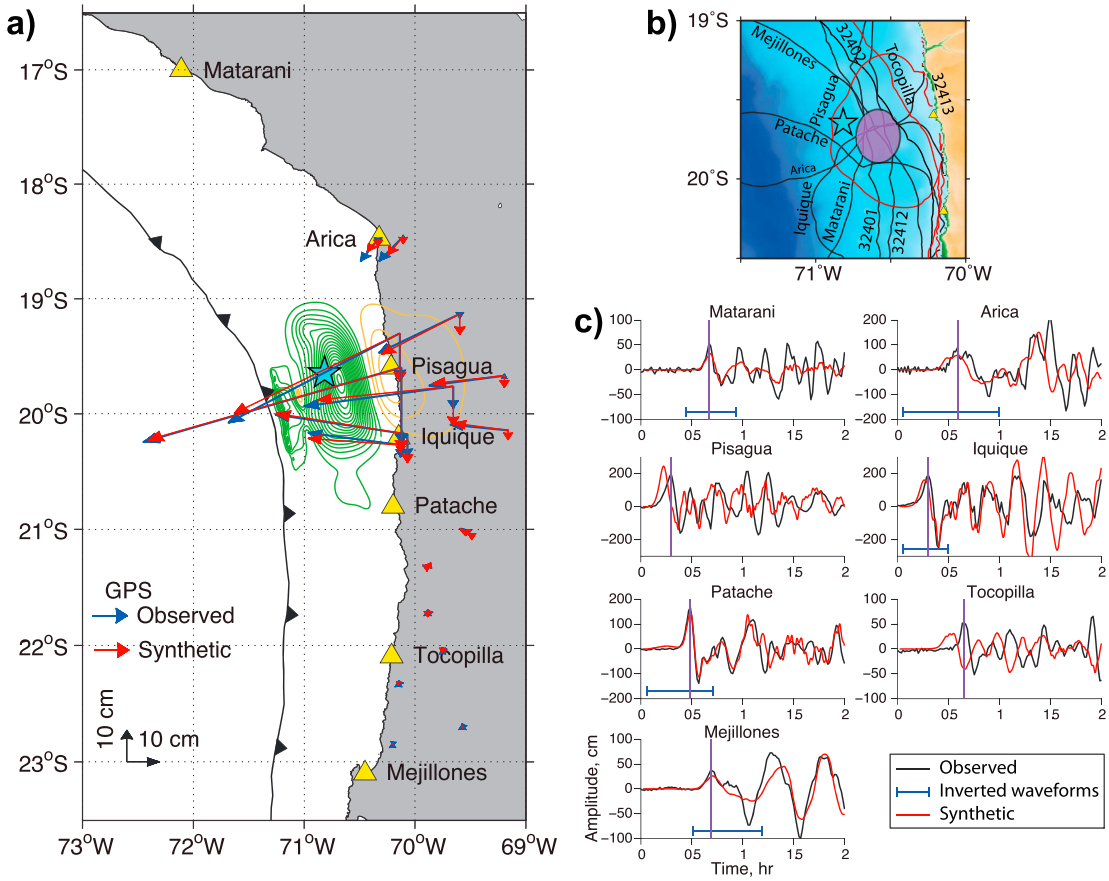

Figure 2. (a) Predicted coseismic crustal deformation from the estimated slip distribution from tsunami waveforms and GPS data (Vr = 1.5 km/s). Red and blue arrows represent the synthetic and observed horizontal and vertical displacements, respectively. Green and orange contours respectively represent positive and negative vertical surface deformation (contour interval = 0.1 m). Yellow triangles represent the tide gauge stations, and the blue star represents the epicenter of the 2014 Iquique earthquake. (b) Travel time map of back-traced tsunami based on the traveltimes of the first peaks of observed tsunami waveforms. Purple area indicates the source area for the first peaks of observed tsunami waveforms. (c) Comparison of synthetic (red lines) and observed (black lines) tsunami waveforms at tide gauge stations. The blue bars indicate the time range used for tsunami waveform inversion. Purple line marks the observed traveltime of the first tsunami peak at each station, which was used for tsunami back tracing (Figure 2b).

wave. In this study, we first use teleseismic body waves to estimate the source time (moment rate) function of the rupture then use the ocean-wide tsunami waveforms and the coseismic displacement data in a joint inversion to estimate the spatial and temporal slip distribution of the 2014 Iquique earthquake.

2. Teleseismic and Tsunami Waveforms and Coseismic Displacement Data

2.1. Teleseismic Waveform Data

We used the teleseismic body waves of 54 *P* wave vertical components recorded at the epicentral distances between 30° and 100° (Figure S1 in the supporting information). We applied a band-pass filter for the frequency range between 0.003 and 1.0 Hz to the original waveforms provided by the Incorporated Research Institutions for Seismology, Data Management Center (IRIS-DMC).

2.2. Tsunami Waveform Data

We used the tsunami waveforms recorded at 19 DART and five tide gauge stations (Figures 1 and 2). The Intergovernmental Oceanographic Commission (IOC) and the National Oceanic and Atmospheric Administration (NOAA) provided the tide gauge and DART data, respectively. To obtain the tsunami waveforms, the ocean tides were approximated by fitting polynomial functions and removed from the original records.

The tsunami was recorded at seven tide gauge stations (Matarani, Arica, Iquique, Patache, Mejillones, Pisagua, and Tocopilla; Figure 2). The highest amplitude of the first tsunami cycles was 187.9 cm at Iquique (Figure 2c). We estimated the tsunami source region by applying Huygens' principle for back tracing the tsunami from each observation station using the Geoware TTT (Tsunami Travel Time) program. The traveltime arcs for the first peaks of Pisagua and Tocopilla were inconsistent with other stations (Figure 2b), probably because of poor bathymetry data around these stations. Hence, we did not use the tsunami waveforms at Pisagua and Tocopilla for the inversion but used them for validation purpose.

Tsunami amplitudes recorded at the DART stations are much smaller because they are located at deep water (3000–6000 m). For example, tsunami amplitude of 24.89 cm was recorded by DART 32401, which is located at a water depth of 4865 m and approximately 290 km from the epicenter (Figures 1a and 1c).

2.3. Coseismic Displacement Data

We used coseismic horizontal and vertical displacements at 13 GPS stations (Figure 2a) of the Integrated Plate Boundary Observatory Chile (IPOC), the International Associated Laboratory, and the Central Andean Tectonic Observatory Geodetic Array projects in northern Chile [*Schurr et al*., 2014]. The horizontal and vertical displacements at stations within 200 km from the epicenter are ranging from 9.0 to 84.7 cm and from −24.4 to 0.4 cm, respectively.

3. Methodology

3.1. Fault Geometry

We assumed a fault with a geometry based on the SLAB1.0 subduction zone model [*Hayes et al*., 2012] and the hypocenter of the aftershocks located by USGS, although the globally estimated depth may not be very accurate (Figure S2). For each subfault, strike angle of 347°, rake angle of 90°, and subfault size of 20 km × 20 km are used.

3.2. Moment Rate Function From Teleseismic Inversion

The moment rate function and the slip distribution were estimated from teleseismic body wave inversion using *Kikuchi and Kanamori*'s [1991] method. The rupture duration on each subfault is decomposed into seven isosceles triangles with duration of 6 s at 3 s intervals, implying that rupture duration for each subfault was at most 24 s. We assumed three different constant rupture velocities, Vr = 1.5, 2.0, and 2.5 km/s, and estimated the moment rate functions and slip distributions.

3.3. Joint Inversion of Tsunami Waveforms and GPS Data

The slip distribution was estimated by a joint inversion of tsunami waveforms recorded at five tide gauge stations, 19 DART stations, and coseismic displacements at 13 GPS stations. We applied a multiple time window inversion [*Satake et al*., 2013] with two time windows with an interval of 15 s allowing each subfault to slip up to 30 s. These parameters were selected so that the total rupture duration of the resulting moment rate function resembles that estimated by teleseismic body wave inversion. Like teleseismic inversion, we assumed three different constant rupture velocities: Vr = 1.5, 2.0, and 2.5 km/s. The Green's functions also contain synthetics of horizontal and vertical displacements at GPS sites. We included a spatial smoothness constraint on the slip distribution into the inversion procedure [*Gusman et al*., 2010].

For the tsunami Green's functions, first we solved the linear shallow water equations and then we corrected the simulated offshore tsunami waveforms by including frequency-dependent dispersion using a method proposed by *Watada et al*. [2014]. The nondispersive linear shallow water equations are numerically solved by a finite different method with staggered grid scheme [*Satake*, 1995]. The bathymetry grid is based on the 30 arc sec General Bathymetric Chart of the Oceans (GEBCO_08) bathymetric data [*Intergovernmental Oceanographic Commission*, *International Hydrographic Organization*, *and British Oceanographic Data Centre*, 2003]. The tsunami waveforms at tide gauges and DART stations are computed on 30 arc sec and 5 arc min bathymetry grids, respectively. The ground deformation from each subfault is computed by *Okada*'s [1985] formula assuming that the solid ocean bottom is modeled as homogeneous elastic half-space. The sea surface deformation is assumed to be the same as the ocean bottom deformation. To include the effects of seawater compressibility, the elasticity of the Earth, and the gravitational potential variation due to the mass motion during the tsunami propagation, we utilized the frequency-dependent phase velocity

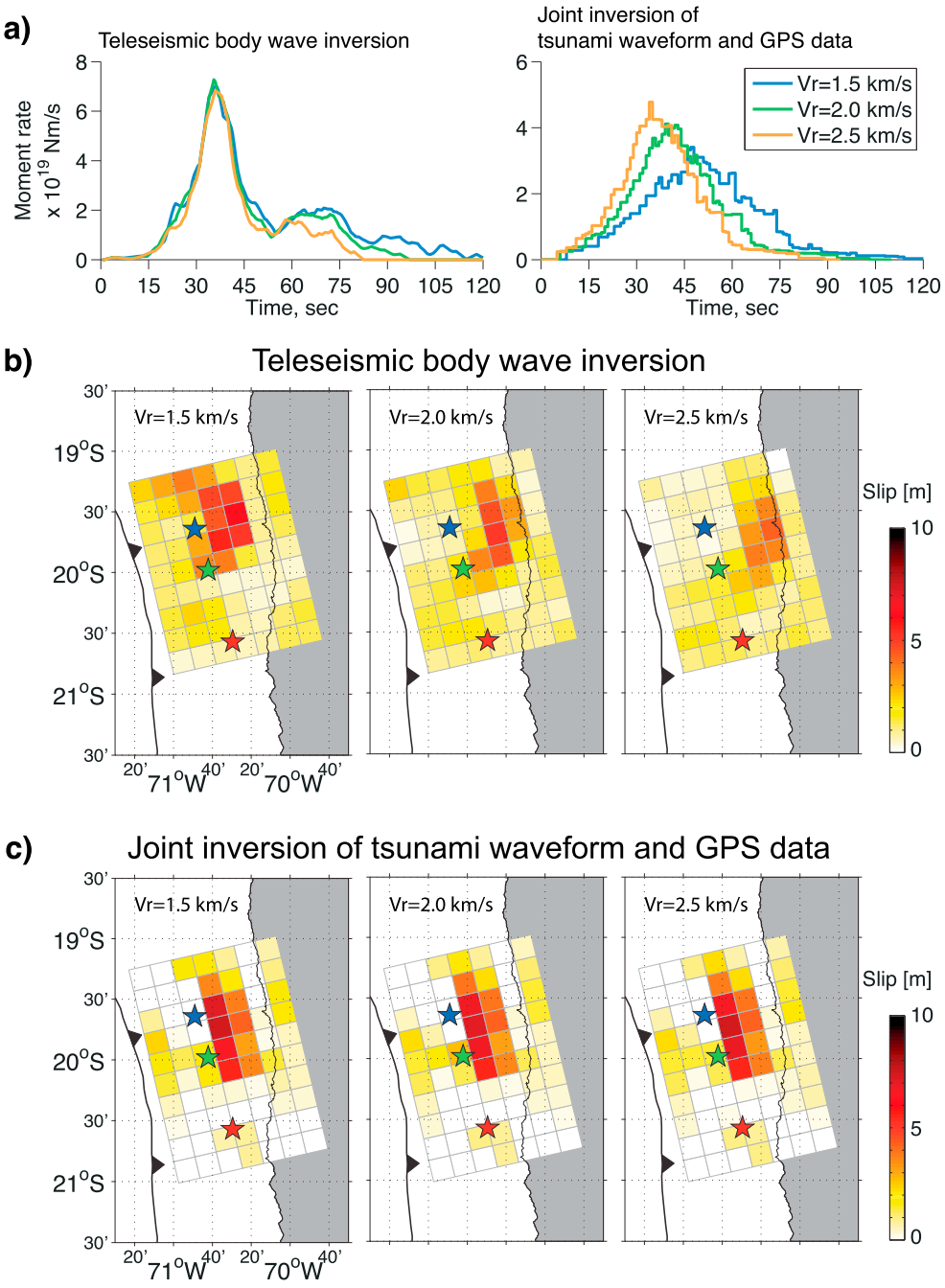

Figure 3. Slip distributions for the 2014 earthquake estimated by teleseismic body wave inversions and joint inversions of tsunami waveforms and GPS data. (a) Moment rate functions from teleseismic body wave inversions and joint inversions of tsunami waveforms and GPS data with assumed constant rupture velocities of 1.5, 2.0, and 2.5 km/s, (b) slip distributions from teleseismic body wave inversions for the assumed rupture velocities, and (c) slip distributions from joint inversions of tsunami waveforms and GPS data for the assumed rupture velocities. Blue, green, and red stars represent the epicenter of the main shock, the largest foreshock, and the largest aftershock, respectively.

computed by the normal mode method [*Watada and Kanamori*, 2010] and corrected the phases of the simulated long-wave tsunami waveforms in the frequency domain by the Fourier transform method [*Watada et al.*, 2014]. With this procedure we account for the fact that waves of different wavelengths travel at different phase velocity. Phase-corrected Green's functions are linear long waves with dispersion effects; hence, any linear inversion scheme for multiple subfaults can be applied.

Because the tsunami amplitudes recorded at DART stations located in the deep ocean are significantly smaller than those at tide gauges, we weighted the tsunami waveforms at DART stations with a factor of 40. The weight factor is 1 for tsunami waveforms at tide gauge stations except for Iquique and Patache where the factor is 3 because the results are very sensitive to these waveforms. The weight factor for the horizontal and vertical displacements data at the GPS stations is 100.

4. Result and Discussion

4.1. Comparison of Teleseismic and Joint Inversion Results

The moment rate functions estimated from the teleseismic body wave inversion with different rupture velocities are quite similar with peaks at ~35 s (Figure 3a). The total rupture duration is different for the assumed rupture velocities, but most seismic moment release ended in ~80 s. This indicates that the teleseismic waveforms provide a robust estimate for the temporal changes of the earthquake source process. The moment rate function estimated from the joint inversion with Vr = 1.5 km/s has a peak at 47 s and the entire rupture process lasted for ~120 s (Figure 3a).

The estimated slip distributions from joint inversion of tsunami waveforms and GPS data are very similar for different rupture velocities (Figure 3c). On the contrary, the spatial slip distributions from teleseismic body wave inversions strongly depend on assumed rupture velocities (Figure 3b). Faster rupture velocity enforces the large slip patch moving toward the deeper part of the fault, beneath the land, although each solution can explain the observed seismic waveforms equally well. Amongst the slip distributions from the teleseismic inversions with the three different rupture velocities, the one for 1.5 km/s is most similar to the slip distribution from the joint inversion of tsunami waveforms and GPS data in terms of large slip area. Thus, the velocity of 1.5 km/s may represent the rupture process of the 2014 Iquique earthquake.

Regardless of the assumed rupture velocities, tsunami waveform misfits from the joint inversions are similar, although the one for the rupture velocity of 1.5 km/s gives the smallest root-mean-square error (RMSE) values (RMSE_Vr1.5 = 0.433, RMSE_Vr2.0 = 0.441, and RMSE_Vr2.5 = 0.443). The RMSE value is larger (RMSE_Vr∞ = 0.476) for the infinite rupture velocity than finite velocities. This may indicate that introduction of finite rupture velocity instead of an instantaneous rupture process can better explain the tsunami waveforms, although they are insensitive to the choice of rupture velocity, as indicated by *Fujii and Satake* [2007]. The tsunami inversion results are insensitive to the assumed rupture velocity because the tsunami phase velocity is only 0.2 km/s at a water depth of 4 km, which is much slower than rupture velocity.

4.2. Rupture Process of the 2014 Iquique Earthquake

The joint inversion of tsunami waveform and GPS data result shows that the 2014 Iquique earthquake ruptured from the epicenter to the southeast direction toward the largest aftershock, which is located on the plate interface that did not rupture during the main shock (Figures 3c and S3). This is consistent with the backprojection result by *Schurr et al*. [2014] and teleseismic inversion result by *Yagi et al*. [2014].

From the slip distribution obtained by the joint inversion of the tsunami and GPS data (Figure 3c and Table S1), the seismic moment (Vr = 1.5 km/s) is calculated as 1.24×10^{21} N m (M_w 8.0) by assuming a rigidity of 4×10^{10} N/m^2. This seismic moment is slightly smaller than that from teleseismic waveform inversion (1.88×10^{21} N m, M_w 8.1). The major slip region with slip amount larger than 3 m extends 100 km × 40 km, and the maximum slip amount is approximately 7 m for both inversions (Figures 3b and 3c). This major slip region is located at downdip side of the hypocenter at depths between 20 and 35 km. The DART data off the coast of Iquique were used; hence, tsunami waveform can better constrain the slip in the shallow region near the trench compared to inversion results of only teleseismic or land-based GPS data. Here we confirmed that the largest slip of the 2014 Iquique earthquake did not reach the plate interface near the trench (Figure 3c).

Tsunami waveforms, land-based GPS data, and teleseismic body waves can provide accurate estimates of offshore slip distribution, slip distribution beneath land, and the precise timing of slip history, respectively, for interplate earthquakes. A slip distribution from only tsunami waveforms (Figure S4) has a very similar pattern to those from the joint inversions. Comparison of the results from the tsunami waveform inversion and joint inversions (tsunami and GPS) show that the tsunami waveform provided strong constraint to the solution, and the GPS data mainly constrain the slip beneath land.

4.3. Tsunami Simulation and Calculated Surface Deformation

The estimated slip distribution from the joint inversion of tsunami and GPS data can explain the observed tsunami waveforms (Figures 1c and 2c) and coseismic displacements (Figure 2a) very well at most stations. Tsunami waveforms at Pisagua and Tocopilla that were not used in the inversion are compared with the simulated ones (Figure 2c). Although the arrival times of the observed and simulated tsunami waveforms at Tocopilla are significantly different, the period and amplitude of first waves are similar.

From the estimated slip distribution, we computed the tsunami waveforms at the DART stations by solving the linear shallow water equations. The arrival time differences between simulated and observed tsunami waveforms are calculated by the cross-correlation technique explained in *Watada et al*. [2014] and shown in Figure 1b. Without the tsunami phase velocity correction, the arrival time differences at stations more than 12000 km away from the source (except for DART 52401) ranged from 10 to 20 min (Figure 1a) or in the range of 1–2% of the traveltime (Figure 1b).

The calculated deformation pattern shows that tide gauge stations located very close to the epicenter (i.e., Pisagua and Iquique) were clearly subsided due to the main shock (Figure 2b). The maximum predicted land subsidence is approximately 30 cm (Figure 2b). While leading positive tsunami waves were recorded at all tide gauge stations (Figure 2c), it does not necessarily mean that there is no subsidence or uplift at near-field stations such as Pisagua, Iquique, and Patache, because tide gauge station and water column move together with the ground during the seismic event.

5. Conclusions

The tsunami arrival time and polarity reversal observed at far-field DART stations can be accurately reproduced by solving shallow water equations and applying the phase velocity correction to the simulated waveforms [*Watada et al*., 2014]. The slip distribution of the 2014 Iquique earthquake from our joint inversion method can accurately explain the tsunami waveform in the near field as well as in the far field. We propose the tsunami phase velocity correction to be included as a standard procedure in inversion methods when using far-field tsunami waveforms.

Inversion of teleseismic body waves provides better temporal resolution, while the joint inversion of tsunami and geodetic data provides a better spatial resolution. Hence, we may reach a more precise time-space distribution and rupture velocity from a combined use of teleseismic body waves, tsunami waveforms, and land-based GPS data. Our result shows that the slip distribution from teleseismic body wave inversion with rupture velocity of 1.5 km/s is consistent with the spatially stable slip distribution from the joint inversion of tsunami waveforms and GPS data.

Acknowledgments

Teleseismic waveforms were downloaded from the Incorporated Research Institutions for Seismology, Data Management Center (IRIS-DMC) website (http://www.iris.edu/wilber3/find_event). Tide gauge and DART data were downloaded from the Intergovernmental Oceanographic Commission (IOC) website (http://www.ioc-sealevelmonitoring.org) and the National Oceanic and Atmospheric Administration (NOAA) website (http://www.ndbc.noaa.gov/dart.shtml), respectively. GPS data were provided by the Integrated Plate Boundary Observatory Chile (IPOC), the International Associated Laboratory, and the Central Andean Tectonic Observatory Geodetic Array projects in northern Chile. The coseismic horizontal and vertical displacements are provided by *Schurr et al*. [2014]. Some of the figures were made using the public domain Generic Mapping Tools [*Wessel and Smith*, 1998]. We thank Hiroo Kanamori for a discussion on slip inversion. We thank Andrew Newman (the Editor) and two anonymous reviewers for their constructive comments.

The Editor thanks two anonymous reviewers for their assistance in evaluating this paper.

References

Allgeyer, S., and P. Cummins (2014), Numerical tsunami simulation including elastic loading and seawater density stratification, *Geophys. Res. Lett.*, *41*, 2368–2375, doi:10.1002/2014GL059348.

An, C., I. Sepúlveda, and P. L.-F. Liu (2014), Tsunami source and its validation of the 2014 Iquique, Chile, earthquake, *Geophys. Res. Lett.*, *41*, 3988–3994, doi:10.1002/2014GL060567.

Fujii, Y., and K. Satake (2007), Tsunami source of the 2004 Sumatra-Andaman earthquake inferred from tide gauge and satellite data, *Bull. Seismol. Soc. Am.*, *97*(1A), 192–207, doi:10.1785/0120050613.

Fujii, Y., and K. Satake (2013), Slip distribution and seismic moment of the 2010 and 1960 Chilean earthquakes inferred from tsunami waveforms and coastal geodetic data, *Pure Appl. Geophys.*, doi:10.1007/s00024-012-0524-2.

Fujii, Y., K. Satake, S. Sakai, M. Shinohara, and T. Kanazawa (2011), Tsunami source of the 2011 off the Pacific coast of Tohoku, earthquake, *Earth Planets Space*, *63*, 815–820, doi:10.5047/eps.2011.06.010.

Gusman, A. R., Y. Tanioka, T. Kobayashi, H. Latief, and W. Pandoe (2010), Slip distribution of the 2007 Bengkulu earthquake inferred from tsunami waveforms and InSAR data, *J. Geophys. Res.*, *115*, B12316, doi:10.1029/2010JB007565.

Gusman, A. R., Y. Tanioka, S. Sakaia, and H. Tsushima (2012), Source model of the great 2011 Tohoku earthquake estimated from tsunami waveforms and crustal deformation data, *Earth Planet. Sci. Lett.*, *341–344*, 234–242, doi:10.1016/j.epsl.2012.06.006.

Hayes, G. P., D. J. Wald, and R. L. Johnson (2012), Slab1.0: A three-dimensional model of global subduction zone geometries, *J. Geophys. Res.*, *117*, B01302, doi:10.1029/2011JB008524.

Heidarzadeh, M., K. Satake, S. Murotani, A. R. Gusman, and S. Watada (2014), Deep-water characteristics of the trans-Pacific tsunami from the 1 April 2014 Mw 8.2 Iquique, Chile earthquake, *Pure Appl. Geophys.*, doi:10.1007/s00024-014-0983-8.

Inazu, D., and T. Saito (2013), Simulation of distant tsunami propagation with a radial loading deformation effect, *Earth Planets Space*, *65*, 835–842, doi:10.5047/eps.2013.03.010.

Intergovernmental Oceanographic Commission, International Hydrographic Organization, and British Oceanographic Data Centre (2003), *Centenary Edition of the GEBCO Digital Atlas*, published on CD- ROM on behalf of the Intergovernmental Oceanographic Commission and the International Hydrographic Organization as part of the general bathymetric chart of the oceans. British oceanographic data centre, Liverpool, U. K.

Kikuchi, M., and H. Kanamori (1991), Inversion of complex body waves—III, *Bull. Seismol. Soc. Am.*, *81*, 2335–2350.
Lay, T., H. Yue, E. E. Brodsky, and C. An (2014), The 1 April 2014 Iquique, Chile, Mw 8.1 earthquake rupture sequence, *Geophys. Res. Lett.*, *41*, 3818–3825, doi:10.1002/2014GL060238.
Lorito, S., F. Romano, S. Atzori, X. Tong, A. Avallone, J. McCloskey, E. Boschi, and A. Piatanesi (2011), Limited overlap between the seismic gap and coseismic slip of the great 2010 Chile earthquake, *Nat. Geosci.*, *4*, 173–177, doi:10.1038/ngeo1073.
Okada, Y. (1985), Surface deformation due to shear and tensile faults in half-space, *Bull. Seismol. Soc. Am.*, *75–4*, 1135–1154.
Rabinovich, A. B., P. L. Woodworth, and V. V. Titov (2011), Deep-sea observations and modeling of the 2004 Sumatra tsunami in Drake Passage, *Geophys. Res. Lett.*, *38*, L16604, doi:10.1029/2011GL048305.
Romano, F., A. Piatanesi, S. Lorito, N. D'Agostino, K. Hirata, S. Atzori, Y. Yamazaki, and M. Cocco (2012), Clues from joint inversion of tsunami an geodetic data of the 2011 Tohoku-oki earthquake, *Sci. Rep.*, *2*(385), 1–8, doi:10.1038/srep00385.
Satake, K. (1995), Linear and nonlinear computations of the 1992 Nicaragua earthquake tsunami, *Pure Appl. Geophys.*, *144*, 455–470.
Satake, K., Y. Fujii, T. Harada, and Y. Namegaya (2013), Time and space distribution of coseismic slip of the 2011 Tohoku earthquake as inferred from tsunami waveform data, *Bull. Seismol. Soc. Am.*, *103*(2B), 1473–1492.
Schurr, B., et al. (2014), Gradual unlocking of plate boundary controlled initiation of the 2014 Iquique earthquake, *Nature*, *512*, 299–302, doi:10.1038/nature13681.
Watada, S., and H. Kanamori (2010), Acoustic resonant oscillations between the atmosphere and the solid earth during the 1991 Mt. Pinatubo eruption, *J. Geophys. Res.*, *115*, B12319, doi:10.1029/2010JB007747.
Watada, S., S. Kusumoto, and K. Satake (2014), Traveltime delay and initial phase reversal of distant tsunamis coupled with the self-gravitating elastic Earth, *J. Geophys. Res. Solid Earth*, *119*, 4287–4310, doi:10.1002/2013JB010841.
Wessel, P., and W. H. F. Smith (1998), New, improved version of generic mapping tools released, *Eos Trans. AGU*, *79*, 579, doi:10.1029/98EO00426.
Yagi, Y., R. Okuwaki, B. Enescu, S. Hirano, Y. Yamagami, S. Endo, and T. Komoro (2014), Rupture process of the 2014 Iquique Chile Earthquake in relation with the foreshock activity, *Geophys. Res. Lett.*, *41*, 4201–4206, doi:10.1002/2014GL060274.